

# Dark Energy from Large-Scale Structure Lensing Information

Tingting Lu,<sup>1,2</sup> Ue-Li Pen,<sup>2</sup> and Olivier Doré<sup>2</sup>

<sup>1</sup>*Department of Astronomy and Astrophysics, University of Toronto, M5S 3H4, Canada*

<sup>2</sup>*Canadian Institute for Theoretical Astrophysics, University of Toronto, M5S 3H8, Canada*

(Dated: April 18, 2022)

Wide area Large-Scale Structure (LSS) surveys are planning to map a substantial fraction of the visible universe to quantify dark energy through Baryon Acoustic Oscillations (BAO). At increasing redshift, for example that probed by proposed 21-cm intensity mapping surveys, gravitational lensing potentially limits the fidelity (Hui et al., 2007) because it distorts the apparent matter distribution. In this paper we show that these distortions can be reconstructed, and actually used to map the distribution of intervening dark matter. The lensing information for sources at  $z = 1 - 3$  allows accurate reconstruction of the gravitational potential on large scales,  $l \lesssim 100$ , which is well matched for Integrated Sachs-Wolfe (ISW) effect measurements of dark energy and its sound speed, and a strong constraint for modified gravity models of dark energy.

We built an optimal quadratic lensing estimator for non-Gaussian sources, which is necessary for LSS. The phenomenon of “information saturation” (Rimes & Hamilton, 2005) saturates reconstruction at mildly non-linear scales, where the linear source power spectrum  $\Delta^2 \sim 0.2 - 0.5$ . We find that steeper power spectra, saturate more quickly. We compute the effective number densities of independent lensing sources for LSS lensing, and find that they increase rapidly with redshifts. For LSS/21-cm sources at  $z \sim 2 - 4$ , the lensing reconstruction is limited by cosmic variance at  $l \lesssim 100$ .

## I. INTRODUCTION

The standard cosmological model has achieved substantial quantitative success through precision cosmology. It requires a mysterious and dominant dark energy component, which is not physically understood. Or it may be a hint that Einstein’s General Relativity is not the correct theory to describe our universe.

New quantitative tests are needed to improve our understanding of the nature of dark energy or modified gravity. In this paper we show how high- $z$  Baryon Acoustic Oscillations (BAO) surveys, in addition to measuring kinematic cosmology, can also constrain the dynamics of perturbations through weak gravitational lensing. A direct measurement of the gravitational potentials can determine the sound speed of the dark energy field [1].

Recently, modified gravity models have been studied quantitatively. In order to pass local precision gravity tests, and match the Cosmic Microwave Background (CMB) fluctuations, these models tend to differ in their predictions only on very large scales and at low redshifts.

Direct all-sky lensing maps are observationally challenging, since the signals are weak, and systematics are difficult to control. However, quadratic estimators of CMB maps have recently demonstrated its feasibility on very large scales [2]. Similar techniques have been proposed for lensing of diffuse structures[3], and will be explored in further detail in this paper.

The kinematic history of the universe is being mapped out using the standard metre stick of BAO. A range of surveys are underway and have been proposed to produce a coarse image of large-scale structure (LSS) over a substantial sky area and redshift range. While these surveys are not directly suitable for lensing mapping, the maps they produce will be distorted by gravitational lensing [4]. Since the intrinsic correlations is known to be statis-

tically isotropic, the lensing induced changes can be used to reconstruct the dark matter map, in analogy with lensing of the CMB. The CMB is a source screen with well known lensing properties, for which lensing and ISW results in a non-zero three point function. As we show in this paper, the kernels are not perfectly matched, and the dynamical dark energy properties can be better measured with sources at a range of redshifts, as is the case for 21cm LSS. This general approach is known as lensing tomography.

Some of the proposed fast BAO surveys [5–7] are based on an intensity mapping approach, where the LSS is mapped without detection of individual galaxies over a large fraction of the sky. For such surveys, point source based lensing mappings are not applicable [8], and the LSS lensing is the only available tool. Lensing reconstruction using Gaussian random fields as sources is now well understood for both 2-D and 3-D structures [3, 9–13]. Metcalf and White [13] have explored the possibility of applying 21-cm lensing from low and high redshifts to the dark energy constraint. While their method is based on the Gaussian assumption, it was shown that the neglect of non-Gaussianity could generate orders of magnitude difference in the noise estimation [12] (hereafter LP08).

In general, lensing reconstruction is a quadratic function of the density field, which is quantified by its power spectrum. Rimes and Hamilton [14] (hereafter RH05) showed that the Fisher information available in the power spectrum saturates at trans-linear scales, and stays several orders of magnitude below the Gaussian Fisher information content. In this paper, we combine the information from these approaches, and construct the optimal quadratic lensing estimators for non-linear sources fields from N-body simulations.

We find that the reconstruction noise of lensing from

the simulated sources decreases with reduced experimental noise at linear scales, saturates at quasi-linear scales, and drops again at highly non-linear scales. There is a plateau region at the trans-linear regime, which is analogous to what was found with the Fisher information content in the initial amplitude of matter power spectrum by Rimes and Hamilton [14]. Both effects are caused by the non-Gaussianity (or non-linearity) introduced by gravitational clustering during structure formation. We found the saturation scale is a steadily increasing function of the shape of the linear power spectrum.

This non-Gaussianity makes the 21-cm lensing less promising than it first appears. However, because of the abundance of 21-cm sources, the Signal-to-Noise ratio (S/N) of 21-cm lensing at high redshift  $z \sim 1 - 6$  is still competitive compared with other surveys. The effective number density of sources defined by the independent number of cells in the 21-cm source, increases quickly with redshift. At redshift 4–6, this number density could be  $9 \text{ arcmin}^{-2}$ .

The paper is organized as follows: We overview the progress in the LSS information and lensing studies in section II. The optimal lensing estimator is introduced in section III. The numerical methods are presented in section IV. The results are discussed in section V. We conclude in section VI.

## II. INFORMATION AND LENSING FROM THE LSS

The lensing of Gaussian random fields can be described in several ways. For the purposes of this paper, we are in a regime where the fluctuation scale of the sources is smaller than the structures of interest in the lenses. In this limit, lensing has two effects on an image: convergence ( $\kappa$ ) and shear ( $\gamma$ ).

As we will find through detailed calculations, these two quantities carry a comparable amount of information, dependent on the slope of the power spectrum of sources. For pedagogical purposes, we first consider the convergence, that is the stretching of the image changes the amplitude of fluctuations at a fixed apparent angular scale. By comparing the power spectrum in different patches, we can measure the relative convergence.

The accuracy of this procedure is proportionate to the precision with which the power spectrum can be measured. This problem has been studied in terms of Fisher Information by RH05, and their results directly translate into the accuracy of lensing reconstruction. After a technical calculation, we find that the effective number of independent lensing sources is equal to the RH05 Fisher Information, scaled by a coefficient of order unity, which depends on the slope of the power spectrum.

A related problem is the impact of lensing on the sky averaged power spectrum [4, 15, 16]. There had been concern that the lensing at low redshift may impact the ability to accurately measure the matter power spectrum

at high redshift. To first order, there is an equal number of positive and negative convergence patches, so the net effect is second order. Since we can measure the first order effect on each patch, we can actually correct its impact, and cancel off the second order bias.

## III. LENSING RECONSTRUCTION

In the lensing of diffuse background, what is observed is the distorted brightness temperature distribution. As discussed in LP08, all lensing estimators are quadratic terms of temperature fields. The lensing field (convergence  $\kappa$ , shear  $\gamma$ , or deflection angle  $\mathbf{d}$ ) can be reconstructed with the product of two smoothed temperature fields. For different estimators, the window functions could also be scalars or vectors.

How to choose the smoothed window is just a matter of optimization. There are also progressive levels of optimization to be considered: Is the source isotropic? Is the window function isotropic? For Gaussian distributed temperature field, the optimal window function can be solved analytically. Hu and Okamoto [17] formulated the optimal quadratic deflection angle estimator (OQDE) for 2-D CMB lensing, and later Zahn and Zaldarriaga [10] generalized it to 3-D 21-cm lensing. The OQDE surprisingly has the same form at all scales, even though an additional scale dependent normalization factor needs to be applied at the last step. In an alternative approach, by optimizing the reconstruction noise in the zero-mode, we derived the optimal Gaussian window for the convergence and shear fields separately in LP08.

In reality, 21-cm sources are not Gaussian fields. For simplicity, we use the 3-D dark matter distribution to represent the 21-cm emission at the same redshift. We investigated both OQDE and our estimators by numerical tests with simulated non-Gaussian source fields and mocked Gaussian ones. For Gaussian sources, we found the combined result of our two estimators has exactly the same S/N as the OQDE on all scales. This agrees with our expectation because of the scale independence of the optimal window functions. If one window function is optimal at one scale, it is also optimal at other scales. For non-Gaussian sources, however, the optimal window function derived from Gaussian assumption is not optimal any more. The lensing reconstruction noise could be underestimated by orders of magnitude if we use the results from Gaussian sources, which could be calculated analytically by applying Wick's theorem. By choosing appropriate weights, our combined estimator has better performance than the OQDE.

In this paper, we will further explore the optimization of non-Gaussian sources. We will develop the optimal non-Gaussian estimator, which can only be constructed by numerical measurements from a large sample of simulations. The reconstruction noise of optimal lensing estimators for non-Gaussian 21-cm sources are closely related to the Fisher information contained in non-linear

matter power spectrum described by RH05. They indicated that the Fisher information for the initial amplitude of matter power spectrum could be written as the sum of the inverse of covariance matrix of power spectrum estimates, multiplied by the partial derivative of power spectrum with respect to the initial amplitude. They have revealed the cumulative Fisher information results up to a maximum scale, which enters the calculation as the upper limit scale of the covariance matrix. They found a very interesting phenomenon: the Fisher information increases at linear scales, and then the growth becomes very slow at the quasi-linear region (which they label as information plateau), and the Fisher information starts to rise again in highly non-linear scales.

In this context, Fisher information means how accurately the amplitude of the power spectrum can be measured. As we will discuss later in section III A, lensing can be detected by the change of the source power spectrum. We will also prove that the optimal window function of non-Gaussian sources actually contains the inverse covariance matrix of power spectra. Thus the reconstruction noise of lensing roughly estimates how much information is contained in the source power spectrum: the lower the noise level achieved, the more information is gained. Instrumental noises of 21-cm experiments can be approximately treated as hard cut-offs at some scales, then we could inspect the reconstruction noises with different cut-off scales. When the sources are Gaussian, the covariance matrix is diagonal and could be expressed as a square term of the source power spectrum, and the optimal window function reverts to the form we found in LP08. Our numerical results with Gaussian estimators had similar behavior as RH05: the reconstruction S/N increased first and reached a peak at trans-linear scales. At non-linear scales, the S/N dropped again. We will explain later, the decline of S/N is an artificial effect by using the non-optimal window function for non-Gaussian sources. In this paper, we will show that the optimal non-Gaussian estimator also leads to a plateau in trans-linear scales in the S/N plot, and like Fisher information of matter power spectrum amplitude, the curve falls again in non-linear scales.

The covariance matrix of non-linear power spectrum is measured from an ensemble of N-body simulations. RH05 showed that the covariance of power spectrum can only be measured with at least hundreds of independent simulations. Therefore we generated around 100 or more different sources, depending on the redshift, by running the same number of N-body simulations.

### A. Optimal non-Gaussian estimator

As we explained in LP08, for the lensing of a diffuse background, all unbiased estimators are two-point functions of the source temperature field with each points convolved with a window function, no matter which quantity is reconstructed: the convergence, shear, de-

flection angle or the potential.

$$E(\mathbf{x}) \equiv \tilde{T}_{w1}(\mathbf{x})\tilde{T}_{w2}(\mathbf{x}), \quad (1)$$

where  $\tilde{T}_{w1}, \tilde{T}_{w2}$  are two convolved temperature fields by some window functions, e.g.,

$$\tilde{T}_{w1}(\mathbf{x}) = \int d^2x' \tilde{T}(\mathbf{x}') W_1(\mathbf{x} - \mathbf{x}'). \quad (2)$$

Here  $\tilde{T}$  is the lensed temperature field, and we use  $T$  to represent the intrinsic unlensed temperature field. We will keep using this convention throughout the paper: the variables with tilde mean the quantities with lensing, while those without tilde mean the original ones. To optimize the estimator, one minimizes its variance

$$\sigma^2(E) = \langle \tilde{T}_{w1}^2 \tilde{T}_{w2}^2 \rangle, \quad (3)$$

which is a four-point function of the temperature distribution. Except for a Gaussian distribution, four-point functions are in general not analytical, and can not be calculated from two-point statistics.

In LP08, we derived optimal estimators of the convergence and shear for a Gaussian source distribution. Since the optimal window function for Gaussian sources (hereafter optimal Gaussian estimator or optimal Gaussian window function) does not depend on the scale, we were able to look for its form in the limit of a slowly varying  $\kappa$  (or  $\gamma$ ). We then applied a maximum likelihood method to solve the optimal window. The calculation was done analytically assuming that the covariance matrix of the power spectrum is diagonal and can be obtained from the power spectrum, which is the implication of Wick's theorem. The variance of optimal Gaussian estimators rises when the resolution of the observation is improved, which shows the optimal Gaussian estimators are far from optimal for a non-Gaussian source distribution.

To find the optimal estimator for non-Gaussian sources, we pursue the calculation in a slightly difference approach. We adopt a minimum variance method, demonstrate it with the Gaussian case and generalize it to the non-Gaussian case. First, we solve the optimal estimator for a constant  $\kappa$  and a Gaussian source, i.e.,  $\kappa(\mathbf{x}) = \kappa_0$ . We then generalize the estimator to the optimal non-Gaussian estimator of varying  $\kappa$  and  $\gamma$ .

The lensed power spectrum from observations can be Taylor expanded in first order as:

$$\begin{aligned} \tilde{P}^{\text{tot}}(\mathbf{k}) &= \tilde{P}(\mathbf{k}) + P^N(\mathbf{k}) \\ &\approx P(\mathbf{k}) + P^N(\mathbf{k}) + \left. \frac{\partial \tilde{P}(\mathbf{k})}{\partial \kappa} \right|_{\kappa=0} \kappa, \end{aligned} \quad (4)$$

where the noise  $P^N = P^e + P^s$  includes both the instrumental noise,  $P^e$ , and the statistical fluctuation of the power spectrum,  $P^s$ , which is the sample variance for a Gaussian source. In LP08, we have defined the derivative of the lensed power spectrum with respect to  $\kappa$ , i.e.,

$G(\kappa, \mathbf{k}) \equiv \frac{\partial \tilde{P}(\mathbf{k})}{\partial \kappa}$ . For convenience, we will use  $G$  to represent its value at  $\kappa = 0$ , therefore

$$G(\mathbf{k}) \approx 2P(\mathbf{k}) + \Delta P(\mathbf{k}), \quad (5)$$

where  $\Delta P = P'k(k_{\perp}^2/k^2)$ ,  $P'(k) = dP(k)/dk$ ,  $k_{\perp}$  means the component of  $k$  in the transverse plane of the line of sight, as defined in LP08. Note that here  $P(\mathbf{k})$  is the expectation value of source power spectrum estimate, and  $\tilde{P}(\mathbf{k})$  is the lensed power spectrum of one realization. In the absence of lensing, the power spectrum in one realization is measured by an estimator  $\hat{P}(\mathbf{k})$ , which is equal to the sum of  $P(\mathbf{k})$  and  $P^N(\mathbf{k})$ . We frequently use the approximation that  $\langle (\tilde{P}^{\text{tot}}(\mathbf{k}) - P(\mathbf{k}))^2 \rangle \approx \langle (\hat{P}(\mathbf{k}) - P(\mathbf{k}))^2 \rangle$  in the reconstruction noise estimation. To simplify the algebra, we first consider the case  $P^e = 0$ , and  $P^N = P^s$ . It will later be straightforward to add the instrumental noise.

### 1. Discrete case

Following the convention of Bertschinger [18], we use subscript  $[\dots]_{\mathbf{k}}$  to describe discrete quantities, and parenthesis  $[\dots](\mathbf{k})$  to describe continuous quantities. For example,

$$\begin{aligned} \tilde{T}(\mathbf{k}) &= \int_{-\infty}^{\infty} d^3x \tilde{T}(\mathbf{x}) e^{-i\mathbf{k}\cdot\mathbf{x}}, \\ \tilde{T}_{\mathbf{k}} &= \sum_j \tilde{T}(\mathbf{x}_j) e^{-i\mathbf{k}\cdot\mathbf{x}_j}. \end{aligned} \quad (6)$$

Note that the observed temperature field is from the contribution of lensed brightness temperature field and noise:  $\tilde{T} = \tilde{T}_b + n$ . The expectation value of the source power spectrum is  $P_{\mathbf{k}} = \langle T_{b\mathbf{k}} T_{b\mathbf{k}}^* \rangle$ , and  $T_{b\mathbf{k}}$  is the discrete Fourier transform of  $T_b(\mathbf{x})$ . If the source brightness temperature follows a Gaussian distribution, the estimators of the unlensed power spectrum  $\hat{P}_{\mathbf{k}}$  at different  $\mathbf{k}$  are independent, and their variance can be calculated as  $\text{Var}(\hat{P}_{\mathbf{k}}) = \langle P_{\mathbf{k}}^N \rangle = \langle P_{\mathbf{k}}^s \rangle = P_{\mathbf{k}}^2/n_{\mathbf{k}_b}$ , where  $n_{\mathbf{k}_b}$  is the number of modes in the  $\mathbf{k}$  frequency bin.

We first consider the discrete case with an independent set of Fourier frequencies  $\mathbf{k}$ . For every frequency, an estimator of  $\kappa$  can be constructed as:

$$\begin{aligned} \hat{\kappa}_{\mathbf{k}} &= \frac{\tilde{P}_{\mathbf{k}}^{\text{tot}} - P_{\mathbf{k}} - P_{\mathbf{k}}^N}{G_{\mathbf{k}}} \\ &= \kappa_0 - n_{\mathbf{k}}, \end{aligned} \quad (7)$$

where  $n_{\mathbf{k}} = P_{\mathbf{k}}^N/G_{\mathbf{k}}$ . Note  $\hat{\kappa}_{\mathbf{k}}$  is not the Fourier transform of  $\hat{\kappa}(\mathbf{x})$ , which has a constant value, but the measurement of  $\kappa_0$  at frequency  $\mathbf{k}$ . The optimal estimator of  $\kappa_0$  should be the total contribution from all  $\mathbf{k}$  appropriately weighted. The minimum variance estimator of  $\kappa_0$  is

$$\hat{\kappa}_0 = \frac{\sum \hat{\kappa}_{\mathbf{k}}/\sigma_{\mathbf{k}}^2}{\sum 1/\sigma_{\mathbf{k}}^2}, \quad (8)$$

where  $\sigma_{\mathbf{k}}^2 = \langle n_{\mathbf{k}} n_{\mathbf{k}}^* \rangle = P_{\mathbf{k}}^2/n_{\mathbf{k}_b} G_{\mathbf{k}}^2$ . Therefore, the weight at each  $\mathbf{k}$  is inverse proportional to the  $\sigma_{\mathbf{k}}^2$ . The reconstruction noise of the minimum variance estimator is now

$$\text{Var}(\hat{\kappa}_0) = \frac{1}{\sum 1/\sigma_{\mathbf{k}}^2}. \quad (9)$$

More generally, in the non-Gaussian case, power spectrum at different  $\mathbf{k}$  are correlated. We can write all variables in the form of matrices and vectors:

$$\mathbf{G}\hat{\kappa}_0 = \tilde{\mathbf{P}}^{\text{tot}} - \mathbf{P} - \mathbf{P}^N, \quad (10)$$

where  $\mathbf{G}$ ,  $\mathbf{P}$  and  $\mathbf{P}^N$  are the  $N_{\mathbf{k}} \times 1$  matrix composed by  $G_{\mathbf{k}}, P_{\mathbf{k}}$  and  $P_{\mathbf{k}}^N$  respectively, and  $N_{\mathbf{k}}$  is the number of all frequencies. The minimum variance (least square) estimator can be written as

$$\mathbf{G}^t \mathbf{C}^{-1} \mathbf{G} \hat{\kappa}_0 = \mathbf{G}^t \mathbf{C}^{-1} (\tilde{\mathbf{P}}^{\text{tot}} - \mathbf{P} - \mathbf{P}^N), \quad (11)$$

where  $\mathbf{C}_{\mathbf{k}, \mathbf{k}'} = \langle P_{\mathbf{k}}^N P_{\mathbf{k}'}^N \rangle$  is the covariance matrix for the power spectrum. Since the terms introduced by lensing do not dominate in the noise, we have neglected their contribution in the covariance matrix  $\mathbf{C}$ . All noise related calculations in the following text will use  $\hat{P}$  instead of  $\tilde{P}^{\text{tot}}$ , while the estimator of lensing quantities will always use  $\tilde{P}^{\text{tot}}$ . Therefore the minimum variance estimator for the non-Gaussian source is

$$\hat{\kappa}_0 = (\mathbf{G}^t \mathbf{C}^{-1} \mathbf{G})^{-1} \mathbf{G}^t \mathbf{C}^{-1} (\tilde{\mathbf{P}}^{\text{tot}} - \mathbf{P} - \mathbf{P}^N). \quad (12)$$

and the variance of the estimator is

$$\text{Var}(\hat{\kappa}_0) = (\mathbf{G}^t \mathbf{C}^{-1} \mathbf{G})^{-1}. \quad (13)$$

### 2. Continuous case

We now consider the continuous case. Assuming the source is a cube with physical length  $L$  in each dimension, by definition  $\tilde{T}(\mathbf{k}) = \tilde{T}_{\mathbf{k}} L^3$ ,  $P(\mathbf{k}) = P_{\mathbf{k}} L^3$ ,  $G(\mathbf{k}) = G_{\mathbf{k}} L^3$  and  $\mathbf{C}(\mathbf{k}, \mathbf{k}') = \mathbf{C}_{\mathbf{k}, \mathbf{k}'} L^6$ . As such, taking the continuum limit leads to

$$\begin{aligned} \hat{\kappa}_0 &= \frac{1}{Q} \int \frac{d^3k}{(2\pi)^3} \frac{d^3k'}{(2\pi)^3} \mathbf{C}^{-1}(\mathbf{k}, \mathbf{k}') G(\mathbf{k}') (\tilde{P}^{\text{tot}} - P - P^N)(\mathbf{k}) \\ &= \int \frac{d^3k}{(2\pi)^3} \tilde{P}^{\text{tot}}(\mathbf{k}) \mathcal{F}(\mathbf{k}) - V, \end{aligned} \quad (14)$$

where

$$\mathcal{F}(\mathbf{k}) = \frac{1}{Q} \int \frac{d^3k'}{(2\pi)^3} \mathbf{C}^{-1}(\mathbf{k}, \mathbf{k}') G(\mathbf{k}'), \quad (15)$$

$$Q = \int \frac{d^3k}{(2\pi)^3} \frac{d^3k'}{(2\pi)^3} \mathbf{C}^{-1}(\mathbf{k}, \mathbf{k}') G(\mathbf{k}) G(\mathbf{k}'), \quad (16)$$

$$V = \int \frac{d^3k}{(2\pi)^3} (P(\mathbf{k}) + P^N(\mathbf{k})) \mathcal{F}(\mathbf{k}). \quad (17)$$

$V$  is the mean variance of the smoothed temperature field. Note that when the source is Gaussian, the optimal filter is  $\mathcal{F}(\mathbf{k}) = G(\mathbf{k})/P(\mathbf{k})^2/Q$ . This is the

estimator presented in LP08. Using  $\tilde{T}(\mathbf{k})\tilde{T}^*(\mathbf{k}) = (2\pi)^3\delta^{3D}(0)\hat{P}^{\text{tot}}(\mathbf{k}) = L^3\hat{P}^{\text{tot}}(\mathbf{k})$  and Parseval's theorem, where  $\delta^{3D}$  is the 3-D Dirac delta function, we can write the calculation in real space instead of Fourier space

$$\begin{aligned}\hat{\kappa}_0 &= L^{-3} \int \frac{d^3k}{(2\pi)^3} \tilde{T}(\mathbf{k})\tilde{T}^*(\mathbf{k})\mathcal{F}(\mathbf{k}) - V \\ &= L^{-3} \int d^3x \tilde{T}_{w1}(\mathbf{x})\tilde{T}_{w2}(\mathbf{x}) - V \\ &= \tilde{T}_{w1}(\mathbf{x})\tilde{T}_{w2}(\mathbf{x}) - V,\end{aligned}\quad (18)$$

where the two window functions to smooth the temperature field are the decomposition of  $\mathcal{F}$ , i.e.,  $W_1W_2 = \mathcal{F}$ . The noise of  $\hat{\kappa}_0$  is

$$\text{Var}(\hat{\kappa}_0) = L^{-6} \int \frac{d^3k}{(2\pi)^3} \int \frac{d^3k'}{(2\pi)^3} \mathbf{C}(\mathbf{k}, \mathbf{k}')\mathcal{F}(\mathbf{k})\mathcal{F}(\mathbf{k}'), \quad (19)$$

where  $\mathbf{C}(\mathbf{k}, \mathbf{k}') = \langle (\hat{P}(\mathbf{k}) - P(\mathbf{k}))(\hat{P}(\mathbf{k}') - P(\mathbf{k}')) \rangle$  is the covariance matrix of the power spectrum. Similar to Eq. (12) in the discrete case, we have neglected the contribution from lensed terms in the estimate of the covariance matrix  $\mathbf{C}$ . It is clear that the noise for  $\hat{\kappa}_0$  equals  $Q^{-1}$ .  $\mathbf{C}(\mathbf{k}, \mathbf{k}')$  will be measured from simulations.

Since

$$\begin{aligned}\tilde{P}(\mathbf{k}_\perp, k_\parallel) &= |\mathbf{J}|^{-1}P(\mathbf{J}^{-1}\mathbf{k}_\perp, k_\parallel) \\ &\approx (1 + 2\kappa)[P(k) + \Delta P(\mathbf{k})(\kappa + \gamma_1 \cos 2\theta_{\mathbf{k}_\perp} \\ &\quad + \gamma_2 \sin 2\theta_{\mathbf{k}_\perp})],\end{aligned}\quad (20)$$

where  $\theta_{\mathbf{k}_\perp}$  is the angle between  $\mathbf{k}_\perp$  and the transverse coordinate (LP08), the first order Taylor expansion gives

$$G^{\gamma_1}(\mathbf{k}) = \Delta P(\mathbf{k}) \cos 2\theta_{\mathbf{k}_\perp}, \quad (21)$$

$$G^{\gamma_2}(\mathbf{k}) = \Delta P(\mathbf{k}) \sin 2\theta_{\mathbf{k}_\perp}. \quad (22)$$

We will rewrite the equation in spherical coordinates using  $\mathbf{k} = (k, \theta, \phi)$ ,  $k_\perp^2/k^2 = \sin^2 \theta$ , and  $\theta_{\mathbf{k}_\perp} = \phi$ .

#### IV. NUMERICAL METHODS

We will calculate the reconstruction noise for sources at redshift: 1.25, 3 and 5. The power spectrum covariance matrix will be measured from N-body simulations. Unless mentioned explicitly, WMAP5 cosmological parameters are used throughout the paper:  $\Omega_m = 0.258$ ,  $\Omega_\Lambda = 0.742$ ,  $\Omega_b = 0.0441$ ,  $\sigma_8 = 0.796$ ,  $n_s = 0.963$ ,  $h = 0.719$ ,  $\tau = 0.087$  [19].

##### A. Simulations

We generate the N-body simulations with the CUBEPM code. CUBEPM is MPI paralleled particle-mesh (PM) code, and has particle-particle forces implemented at sub-grid scales. It is further parallelized by

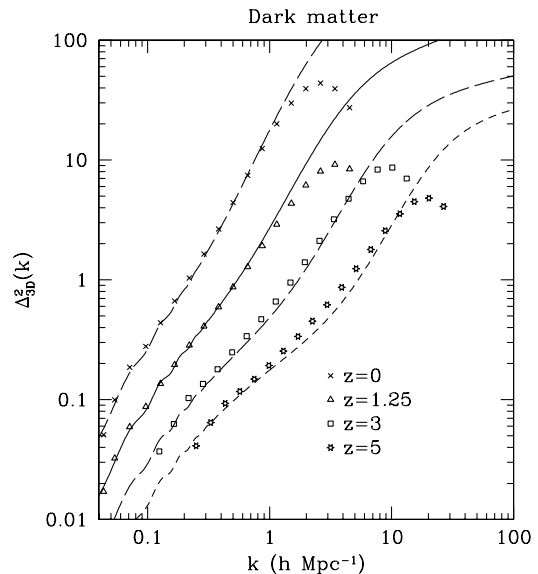


FIG. 1: Power spectrum at  $z=0, 1.25, 3,$  and  $5$ . The data points are from simulations, and the lines are the predicted non-linear power spectra generated by CAMB. The non-linearity increases with lower redshift. The power spectra from simulations at small scales drop due to the resolution limits. The parameters of the simulations are shown at table I.

shared-memory OpenMP on each node. The simulation volume (which is also called simulation box) is cubically decomposed to  $n^3$  sub-volumes, and the calculation of each sub-volume is performed on one node of cluster. The total number of nodes used in simulation is  $n^3$ . The code has been run on up to 1000 nodes. We used  $n = 2$  and  $3$  in our simulations. The simulations are run on the SUNNYVALE cluster of Canadian Institute for Theoretical Astrophysics (CITA), which is a Beowulf cluster composed of 200 Dell PE1950 nodes. For each node there are 2 quad core Intel(R) Xeon(R) E5310 @ 1.60GHz processors, 4GB of RAM, and 2 gigE network interfaces.

HI gas is distributed in galaxies. If we ignore the bias between the galaxies and dark matter distributions, we could approximately use dark matter to represent 21-cm sources distributions at these redshifts (the simple toy model in LP08) since HI sources are expected to trace dark matter fairly well. We have generated the source distribution with CUBEPM and we output the 3-D particles distribution at redshifts 1.25, 3 and 5. To correctly measure the covariance matrix of power spectrum, we generate 186 independent simulations at  $z = 1.25$ . Because the non-linearity is less at higher redshift, we have run 100 simulations at  $z = 3$  and 90 simulations at  $z = 5$ . The density field is produced by assigning the mass of particles to nearby grids with Cloud in Cell (CIC) method.

As we will illustrate later, the 3-D Fisher information (as defined in RH05) of the amplitude of source power spectrum has similarity with the reconstruction noise.

redshift	$L(h^{-1} \text{Mpc})$	$\Delta^2(2\pi/L)$	$n_{grid}$	$\Delta^2(k_{Ny})$	$k_s$	$\Delta_{lin}^2(k_s)$
0	300	0.012	512	219	0.14	0.46
1.25	300	0.0036	512	39.3	0.28	0.34
3.0	100	0.015	1024	40.5	0.47	0.19
5.0	50	0.020	1728	26.5	0.99	0.16

TABLE I: Source simulation parameters. We choose these simulations to optimize the computation load while maintaining the required resolution. The simulation parameter choice is validated by looking at the convergence of the Fisher information content of the power spectrum in both linear and non-linear scales. We found the upper limit for the non-linear power spectrum at the fundamental modes, which has the same size as the box, is around 0.02; and the lower limit for non-linear power spectrum at the Nyquist frequency  $k_{Ny}$ , is around 20. The values of non-linear power spectra are estimated from CAMB.  $k_s$  are the saturation scales of the Fisher information, as shown in Fig. 2. We also list the values of the linear power spectra at these saturation scales for all four redshifts.

We thus address the convergence as a function of the number of simulations with a Fisher information plot. We check the values of  $\sum_{k,k' \leq k_{max}} \bar{\mathbf{C}}_{k,k'}^{-1}$ , where  $\bar{\mathbf{C}}$  is the covariance matrix of the normalized power spectrum  $P(k)/\langle P(k) \rangle$ , that is, the Fisher information is inversely proportional to the variance of the amplitude of normalized power spectrum. We have considered runs with different resolutions and box-sizes for each redshift. The box-size needs to be big enough so that not much of the linear modes are cut-off by the limited box-size. On the other hand, the non-linear structure needs to be resolved at small enough scales so that the saturation effect can be seen. We confirmed the convergence at linear scales by comparing the results with the Gaussian prediction, and at non-linear scales by comparing with higher resolution simulations. We found the upper limit for the non-linear power spectrum at the fundamental modes, which has the same size as the box, is around  $\Delta^2 \lesssim 0.02$ ; and the lower limit for non-linear power spectrum at the Nyquist frequency  $k_{Ny}$ , is around  $\Delta^2 \gtrsim 20$ . The simulations parameters we finally chose are given in table I, and the power spectra are shown at Fig. 1. The values of the non-linear power spectrum are estimated from CAMB, and thus can be obtained before running simulations. The actual power spectra from N-body simulations are always lower than that at  $k_{Ny}$  because of the finite resolution. The sources at  $z = 1.25$  are produced with simulations with  $300h^{-1}\text{Mpc}$  box, and  $256^3$  particles on  $512^3$  grids. For  $z = 3$ , because the matter distribution is more linear, we need to increase the resolution to reach the non-linear structures at smaller scales. We did this by using a smaller box with  $L = 100h^{-1}\text{Mpc}$  and more refined grids with  $n_{grid} = 1024$ . At  $z = 5$ , the non-linearity is lower, and we choose a  $50h^{-1}\text{Mpc}$  box with  $1728^3$  grids. For the sources at  $z = 3$  and  $z = 5$ , we have assigned the particles distributions to  $512^3$  grids though the N-body simulations were performed on finer meshes for the sake of computation efficiency. We also include the Fisher information at  $z = 0$ , using the same simulation parameters as those at  $z = 1.25$ .

The inversion of a large covariance matrix with a few hundred of elements on each dimension can be numerically challenging. Following RH05, we divide the power

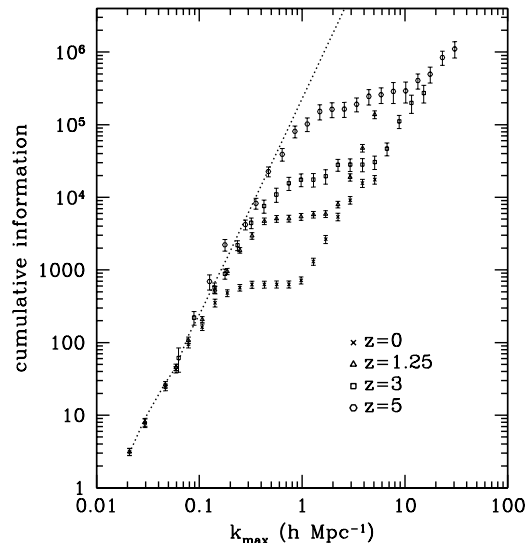


FIG. 2: The 3-D Fisher information content of the amplitude of power spectrum at  $z = 0, 1.25, 3.0, 5.0$  respectively. All results are normalized to the values for a  $300h^{-1}\text{Mpc}$  box. The dashed line is the Gaussian prediction. It is clear that the Fisher information curves grow as  $k^3$  at linear scales, then turn flat at quasi-linear scales ( $k \sim 0.5 - 2h\text{Mpc}^{-1}$  for  $z = 1.25$ ), before going up again at non-linear scales. As expected, there is a gradual evolution of the plateau from  $z = 0$  to  $z = 5$ .

spectra to  $N_b = 20$  bins uniformly distributed in log scale, and calculate the associated band power spectra and their covariance matrix. Subsequently, we invert the  $N_b \times N_b$  matrix instead. The Fisher information can be seen in Fig. 2. All results are normalized for a  $300h^{-1}\text{Mpc}$  box, i.e., multiply the Fisher information measured by  $(300/L)^3$  because larger volume has more independent modes. It is clear that the Fisher information curves grow as  $k^3$  at linear scales, then turn flat at quasi-linear scales ( $k \sim 0.5 - 2h\text{Mpc}^{-1}$  for  $z = 1.25$ ), before going up again at non-linear scales with a quasi-Gaussian scaling. There is a gradual evolution of the plateau from  $z = 0$  to  $z = 5$ .

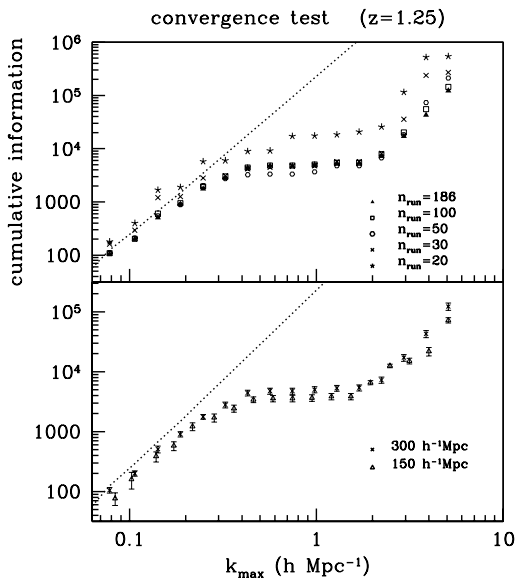


FIG. 3: Convergence test of the Fisher information as a function of simulations. We increase the number of simulations in the top panel. The relative difference from the 186 runs result is 2% for 100 runs, and 10% for 50 runs. When the number of simulations is less than 30, the deviation is comparable to the Fisher information itself. The bottom panel is for different box-sizes, both types have 186 runs. The error bars are generated by the bootstrap method. The Fisher information from simulations with  $L = 150h^{-1}$  Mpc agrees reasonably well with the one from  $300h^{-1}$  Mpc simulations. As such, the lower limit of power spectrum at fundamental mode should be equal to or higher than the value found in the  $150h^{-1}$  Mpc simulations.

We show the convergence of the Fisher information as a function of both the number of simulations  $n_{\text{sim}}$  and the resolution in Fig. 3. In the top panel,  $n_{\text{sim}}$  are reduced from 186 to 100, 50, 30 and 20. The relative difference from the 186 runs result is 2% for 100 runs, and 10% for 50 runs. When the number of simulations is less than 30, the deviation is comparable to the Fisher information itself. We emphasize here that the required number of simulations also depends on the number of bins  $N_b$ :  $N_b$  has to be much smaller than the number of simulations for the covariance matrix to be non-singular. In the bottom panel, we show the convergence of two sets of simulations with different box-sizes. Both types have 186 runs. The Fisher information from simulations with  $L = 150h^{-1}$  Mpc agrees reasonably well with the one from  $300h^{-1}$  Mpc simulations. We thus deduce that the lower limit for the power spectrum at fundamental mode should be equal to or higher than the value found in the  $150h^{-1}$  Mpc simulations.

## B. Lensing reconstruction

We now study the lensing reconstruction noise that will be measured directly from reconstructed lensing maps

with the optimal quadratic estimator described in section III.

### 1. Power spectrum covariance matrix

The power spectrum covariance matrix can be written as  $\langle P(\mathbf{k})P(\mathbf{k}') \rangle - \langle P(\mathbf{k}) \rangle \langle P(\mathbf{k}') \rangle$ . Because the source is isotropic and stationary,  $\langle P(\mathbf{k})P(\mathbf{k}') \rangle$  can be expressed in a symmetric way  $\mathbf{C}(k, k', \cos \theta_{\mathbf{k}, \mathbf{k}'})$ , where  $\cos \theta_{\mathbf{k}, \mathbf{k}'}$  is the angle between the two vectors on the two shells denoted by  $k$  and  $k'$ . We can then expand  $\mathbf{C}$  in spherical harmonic functions, and because it is independent of  $\phi$ , the expansion can be written as the sum of the Legendre functions

$$\mathbf{C}(k, k', \cos \theta_{\mathbf{k}, \mathbf{k}'}) = \sum_{l=0}^{\infty} \mathbf{C}_l(k, k') P_l(\cos \theta_{\mathbf{k}, \mathbf{k}'}). \quad (23)$$

Here  $l$  is a even integer because  $\mathbf{C}(k, k', \cos \theta_{\mathbf{k}, \mathbf{k}'})$  is an even function of  $\theta$ . The window function can be written as an integral of the form

$$\mathcal{F}^{\kappa}(\mathbf{k}) \propto \int \frac{d^3 k'}{(2\pi)^3} \mathbf{C}^{-1}(\mathbf{k}, \mathbf{k}') [G_0^{\kappa}(\mathbf{k}') + G_2^{\kappa}(\mathbf{k}')], \quad (24)$$

where

$$G_0^{\kappa}(\mathbf{k}) = 2P + 2P'k/3, \quad (25)$$

$$G_2^{\kappa}(\mathbf{k}) = P'k(-\cos^2 \theta_{\mathbf{k}'} + 1/3), \quad (26)$$

which are proportional to the zeroth order and second order Legendre function  $P_0(\cos \theta_{\mathbf{k}'})$  and  $P_2(\cos \theta_{\mathbf{k}'})$ . For each  $\mathbf{k}$ , we can always choose the z-axis along it so that  $\cos \theta_{\mathbf{k}, \mathbf{k}'}$  is equal to  $\cos \theta_{\mathbf{k}'}$  without loss of generality. Because the orthogonal property of the Legendre functions, only zeroth and second terms in  $\mathbf{C}^{-1}$  remain, all the higher orders cancel out by the integral over  $\mathbf{k}'$ .

In other words, we decompose the optimal window function in two orthogonal components from the zeroth and second order of the covariance matrix expansion terms respectively. For Gaussian sources, the power spectrum modes are uncorrelated with other modes in different directions or on different shells, therefore all  $\mathbf{C}_l$  are equal. For non-Gaussian sources,  $\mathbf{C}_2$  is about an order of magnitude higher than  $\mathbf{C}_0$ , so the additional information of lensing obtained by using  $\mathbf{C}_2$  is negligible (private communication with Joachim Harnois-Deraps, Harnois-Deraps et al. [20]).

In Fig. 4, we show the optimal non-Gaussian window, and the optimal Gaussian window function in Fourier space. The latter window has an almost power-law slope, while the former one has both positive and negative values due to the complicated behavior of inverse covariance matrix  $\mathbf{C}^{-1}$ . We use crosses to represent the absolute values of the negative part of the optimal non-Gaussian window.

In this paper, we will reconstruct the estimator using the zeroth order only. Modes on a shell can be binned as

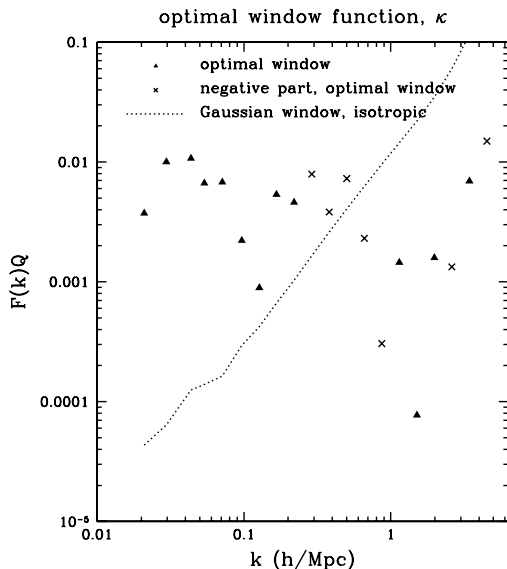


FIG. 4: The optimal non-Gaussian window, and the optimal Gaussian window function in Fourier space. The latter window has an almost power-law slope, while the former one has both positive and negative values due to the complicated behavior of inverse covariance matrix  $\mathbf{C}^{-1}$ . We use crosses to represent the absolute values of the negative part of the optimal non-Gaussian window.

a group first. We could simplify the estimator by calculating its 1-D equivalent, e.g., replacing  $P(\mathbf{k})$  with  $P(k)$ . Working in lower dimension facilitates the numerical calculation, especially the inversion of covariance matrix. Rather than working with a 6-D array  $\mathbf{C}(\mathbf{k}, \mathbf{k}')$ , we now only need to calculate the covariance matrix

$$\mathbf{C}(k, k') = \langle P(k)P(k') \rangle - \langle P(k) \rangle \langle P(k') \rangle. \quad (27)$$

We treat the modes on each  $k$  shell as independent components and the window function corresponding to this shell is calculated from the overall contribution of these modes. We use another trick in the calculation of window function by replacing  $\sum \mathbf{C}^{-1}(\mathbf{k}, \mathbf{k}')G(\mathbf{k}')$  with  $\sum \mathbf{C}_0^{-1}(k, k')G_0(k')$ .

When considering the shear, the calculation is very similar.  $G^{\gamma_1} = P'k \sin^2 \theta \cos 2\phi$  can also be written as the sum of Legendre functions:

$$G_0^{\gamma_1} = 2P'k \cos 2\phi/3, \quad (28)$$

$$G_2^{\gamma_1} = P'k(1/3 - \cos^2 \theta) \cos 2\phi. \quad (29)$$

Therefore only the zeroth and second order mode of covariance remain, and we will also just use the zeroth order in the reconstruction of  $\gamma_1$ . For  $\gamma_2$ , one just need to replace  $\cos 2\phi$  by  $\sin 2\phi$ . The convergence can be calculated from the reconstructed shear. We will call this convergence,  $\gamma_E$ . Similar to LP08, we can choose the axis of the coordinate to be parallel to the direction of the mode measured, so that  $\gamma_E = \gamma_1$ .

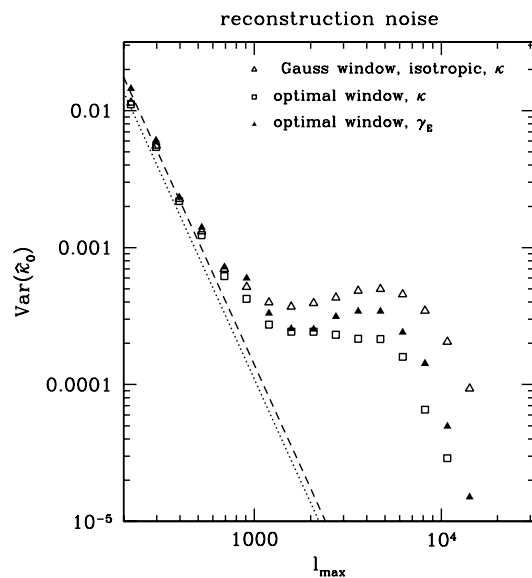


FIG. 5: The contribution from one box at  $z = 1.25$  to the variance of various estimators. The variances are averaged over 186 independent boxes. The reconstruction noises for the Gaussian window, the optimal window for  $\kappa$ , and the optimal window function for  $\gamma_E$  are presented. At linear scales, i.e., when  $\ell < 1000$ , the two estimators have the same reconstruction noise. The non-Gaussian window has a factor of a few less noise than the Gaussian estimator, and displays a plateau above the saturation scale. The plateau means that the non-Gaussianity of sources caused by the effective number of cells increases slowly below the saturation scales, i.e., the structures are intrinsically correlated below such scales and external factor such as experimental noise will not have much effect. The Gaussian estimator used in LP08 does not decrease at saturation scale, and even starts to increase at smaller scales. This is an artifact of the non-optimality of the Gaussian estimator for non-Gaussian sources. We also show the results from Gaussian sources as dashed (shear) and dotted lines (convergence). The slight non-monotonicity in the shear variance probably comes from the dropping of the quadrupolar  $C_2$  term (see text).

## 2. Convolution

The optimal estimator contains the inverse covariance matrix  $\mathbf{C}^{-1}$ , which we measure using around 100 – 200 sources. For  $512^3$  grids, there are about 256 modes covering the range from the box-size scale to the Nyquist scale. The inversion of the  $256 \times 256$  covariance matrix will be unstable, because the number of eigenvalues is more than the total number of independent samples. As such, we will keep using the 20 bins in our calculation. The binned window function are less optimal, but the difference is a minor disadvantage compared to the stability of the inversion. Another important term in the window function is the gradient of the power spectra. Since the power spectrum is close to a power-law, we calculate the gradient by finding the tangent of the power spectrum at saturation scale  $k_s$  measured from the Fisher information on the log-log plot. We find  $P'k = n_{\text{NL}}P$ , and  $n_{\text{NL}} = -1.6, -1.9$  and  $-2.1$  for  $z = 1.25, 3$  and  $5$  respec-



tively.

On the  $512^3$  grids, we calculate the window function with the band power, inverse matrix, and gradient. The Nearest Grid Point (NGP) method is used to map these band values to the 3-D grids in Fourier space. From Eq. (20), we know that the optimal window function does not only depend on the amplitude  $k$ , but is also a function of  $k_\perp$ . Note that when considering the shear, there is an extra angular dependence on  $\theta_{\mathbf{k}_\perp}$ , the direction on the transverse plane that we need to take into account when computing the window function.

Finally, the 3-D sources are convolved with the optimal window function. Since the window functions are generated in Fourier space, we can simply transform the temperature fields to Fourier space by Fast Fourier Transform (FFT), multiply by the window functions, and transform them back to real space.  $\kappa$  or  $\gamma_E$  maps are integrals of the covariance maps of the two convolved fields along the line of sight. Since we are interested in the zero mode, which is the average value of the covariance, we calculate the reconstruction noise of the combined estimator of  $\kappa$  and  $\gamma_E$  (as in LP08), which decrease the noise level. To validate the procedure, we compare the reconstruction noises with the analytical predictions in the Gaussian simulations with the same power spectra as the simulated sources.

## V. NUMERICAL RESULTS AND DISCUSSION

### A. Reconstruction noise

The optimal estimators were derived in the constant  $\kappa(\gamma)$  limit (zero-mode). For the other scales, we need to scale the estimator by a normalization factor  $b(\ell)$ . The derivation of  $b(\ell)$  can be found in appendix A. Not surprisingly,  $b(\ell) \leq 1$ , and decreases from 1 to 0 when  $\ell$  increases, for any given estimator. For the scales we are interested in – above the characteristic scale  $\ell_a$  –  $b(\ell)$  is close to 1, and the noise properties are similar to the zero-mode one. To illustrate the comparison between different estimators at various  $\ell$  with the of zero-mode reconstruction, we treat the experimental noise as a hard cut-off at  $k_c$ .  $\ell_a \sim \ell_c/2 = \chi(z_s)k_c/2$ . This is motivated by the fact that the reconstructed noise is proportional to  $k^{-3}$  on linear scales, and the contribution to the reconstruction at  $k \leq k_c/2$  are small and can be treated like the zero-mode. The values of  $\ell_a$  are shown in Fig. 8 and 9.

In Fig. 5, the zero-mode  $\kappa$  reconstruction noises from various estimators are presented as functions of various cut-off scales at  $z = 1.25$ . For this plot, the noises correspond to the contribution from a single simulation box of width  $300h^{-1}\text{Mpc}$ , and is measured over 186 independent boxes. As a reference, we present the reconstruction noises from the Gaussian window, non-Gaussian window for  $\kappa$  and the non-Gaussian window for  $\gamma_E$ . On linear scales, i.e., when  $\ell < 1000$ , the two estimators of  $\kappa$  have the same reconstruction noise. At smaller scales,

the non-Gaussian window reduces the noise by factor of a few compared to the Gaussian estimator, and has a plateau after the saturation scale. The experimental noise smears out the structure in the sources, and regions which are originally independent become correlated. In other words, lower noise level leads to a larger effective number of independent source cells. Similarly, the effective number of cells increases if the experiment is resolved at smaller scales, therefore the reconstructed noise is lower. The plateau means that the non-Gaussianity of sources cause the effective number of cells to increase very slowly below the saturation scale, i.e., the structures are intrinsically correlated below this scale and external factors such as experimental noise will have little effect. The Gaussian estimator we used in LP08 also saturates at saturation scales, and even increases at smaller scales. This is an artifact effect coming from the fact that the Gaussian estimator is non-optimal for non-Gaussian sources. Note also that shear has better S/N level than  $\kappa$ . To compare with the simulated sources, we also show the results from Gaussian predictions calculated using Wick's theorem. In fact, the reconstruction noises in the Gaussian case can be approximated by the following power-law relationship:

$$\begin{aligned} \text{Var}(\kappa_0^{Gauss}) &\approx 3\pi^2 L^{-3} k_c^{-3} \left(1 + \frac{n_{\text{NL}}}{3}\right)^{-2}, \\ \text{Var}(\gamma_{E0}^{Gauss}) &\approx 45\pi^2 L^{-3} k_c^{-3} n_{\text{NL}}^{-2}. \end{aligned} \quad (30)$$

Note that  $n_{\text{NL}}$  can not be -3 or 0, otherwise the variance of the estimator is infinity and the lensing signal can not be reconstructed. An intuitive explanation is that, in these cases the variance of temperature field are conserved even after being lensed, therefore lensing maps can not be distinguished from unlensed ones and lensing can not be extracted. This stems from the fact that we only consider the zero order,  $\mathbf{C}_0$ , in the covariance matrix of matter power spectrum. Lensing can still be solved for  $n_{\text{NL}} = -3, 0$  cases if  $\mathbf{C}_2$  is taken into account in the estimator.

### B. Saturation effects

We define the saturation scale  $k_s$  as the wavenumber where the noise from the Gaussian prediction is equal to the average amplitude of reconstructed noise in the plateau. We have discussed the saturation effects of lensing reconstruction in LP08, where we found that at  $z = 7$  the S/N saturates at the equivalent scale  $k_s$  where the non-linear power spectrum of source  $\Delta^2(k_s) \sim 0.2$ . The corresponding linear power spectrum at  $k_s$  is about 0.17, which is consistent with the results at other redshifts shown in table II. It is not clear why the value of  $\Delta_{lin}^2(k_s)$  is slightly higher at  $z=7$ . It could come from either the fact that there were less sources ( $n_{sim} = 20$ ) or that the estimator was less optimal in the works of LP08. Note that since we used a Gaussian estimator in LP08 and no

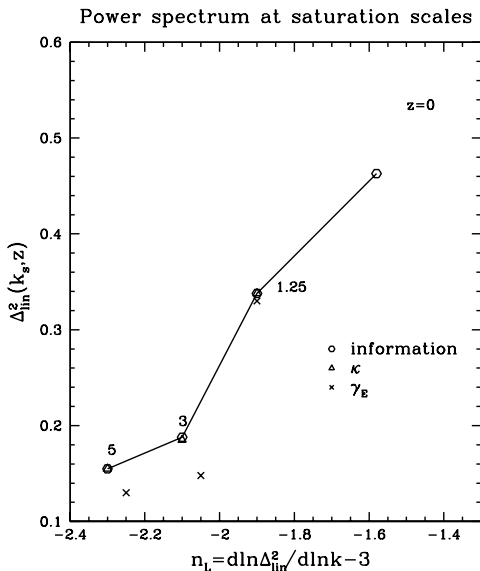


FIG. 6: Power spectra at the saturation scales of the lensing reconstruction noises for different redshifts. It can be seen that  $\Delta_{lin}^2(k_s)$  increases with steeper shape of power spectrum. The points measured from the  $\kappa$  saturation almost overlap with those measured from the Fisher information saturation because the shapes of the source power spectra are very close to power-laws.

$C^{-1}$  term was involved, the convergence of the reconstructed noise should be much better than that for the Fisher information shown in Fig. 3. Since the shape of the matter power spectrum persists except the non-linear scales shift to larger scales, we expect to see similar saturation effects at lower redshifts. This is confirmed by Fig. 5 and later by Fig. 6.

As we mentioned earlier, the saturation effect resembles the Fisher information saturation effect for the initial amplitude of the 3-D dark matter power spectrum in RH05. Their cumulative Fisher information increases at linear scales. On trans-linear scales, the Fisher information is degenerate with that from larger scales and the cumulative Fisher information does not increase. It is possible to view their Fisher information as a special case of our lensing reconstruction calculation if the gradient term  $G$  equals the derivative of the power spectrum with regard to an overall amplitude. Neyrinck et al. [21] have used halo models to explain this saturation effect: on linear scales, the cumulative Fisher information increases with higher  $\ell$ , as the volume and number of halos do. On trans-linear scales, the 2-halo term first dominates, which washes out the fluctuation in 1-halo term. On non-linear scales, the contribution from small mass halos dominates, and the Fisher information increases again – at less than 1% of the Gaussian information. Our numerical results confirmed the reports of RH05.

The saturation scales, as well as the non-linear scales, change with redshifts. To illustrate this we investigate the evolution of  $\Delta_{lin}^2$  at the saturation scale. In Fig. 6,

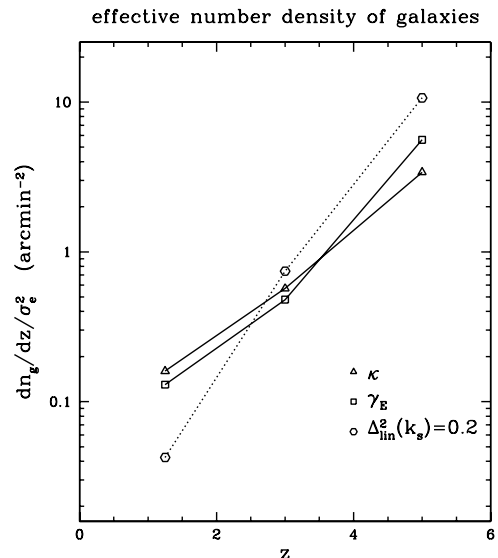


FIG. 7: The effective number densities of sources at various redshifts. When the redshift is higher, the non-linearity of sources goes down.  $dn_g/dz/\sigma_e^2$  increases quickly with redshift. We also plot the number density for a toy model where  $\Delta_{lin}^2(k_s) = 0.2$  for all redshifts.

we plot  $\Delta_{lin}^2(k_s)$  at three redshifts and we give the corresponding numbers in table II. Because the optimal estimator is a function of the gradient of the power spectrum, we will try to see the evolution of  $\Delta_{lin}^2(k_s)$  with the gradient of power spectrum at the saturation scale. It can be seen that  $\Delta_{lin}^2(k_s)$  increases with steeper shape of power spectrum. The points from  $\kappa$  almost overlap with those from the Fisher information, because the shapes of source power spectra are very close to power-laws.

### C. Effective number density

To describe the information content gained in the 21-cm lensing in a more intuitive way, we define  $n_g$ , the equivalent effective surface number density of galaxies which gives the same noise level at the scale where  $S/N$  equals to one:

$$\text{Var}(\hat{\kappa}) = \frac{\sigma_e^2}{n_g \cdot \text{Area}} \approx \frac{1}{N_{cell}}. \quad (31)$$

Similarly, we can define the number of effective independent cells,  $N_{cell}$ , and an effective number density for the noise of  $\gamma_E$ . The characteristic scale of the independent cell is approximately the saturation scale  $k_s$ . The cell size is

$$L_{cell} = 2\pi/k_s \times [27(n_{NL} + 3)^{-2}/8\pi]^{1/3}, \quad (32)$$

$$L_{cell} = 2\pi/k_s \times [45n_{NL}^{-2}/8\pi]^{1/3} \text{ for } \gamma_E, \quad (33)$$

redshift	estimator	$dn_g/dz/\sigma_e^2$ (arcmin $^{-2}$ )	$L_{cell}$ ( $h^{-1}$ Mpc)	$\ell_s$	$k_s$	$\Delta_{lin}^2(k_s)$
1.25	$\kappa$	0.16	19.	773	0.28	0.34
1.25	$\gamma_E$	0.13	20.	773	0.28	0.34
3.0	$\kappa$	0.57	13.	2136	0.46	0.19
3.0	$\gamma_E$	0.48	14.	1671	0.36	0.15
5.0	$\kappa$	3.4	7.0	5657	0.99	0.16
5.0	$\gamma_E$	5.6	5.9	4514	0.79	0.13

TABLE II: Equivalent number densities of galaxies and saturation scales at different redshifts. The characteristic scale of the independent cell  $L_{cell}$  is approximately the saturation scale  $k_s$ . The number density  $n_g$  is calculated with Eq. (31). Because  $n_g$  itself depends on the box-size of the simulated source and the variance of intrinsic ellipticities  $\sigma_e^2$ , we compare  $dn_g/dz/\sigma_e^2$  instead, which increases rapidly with redshift.

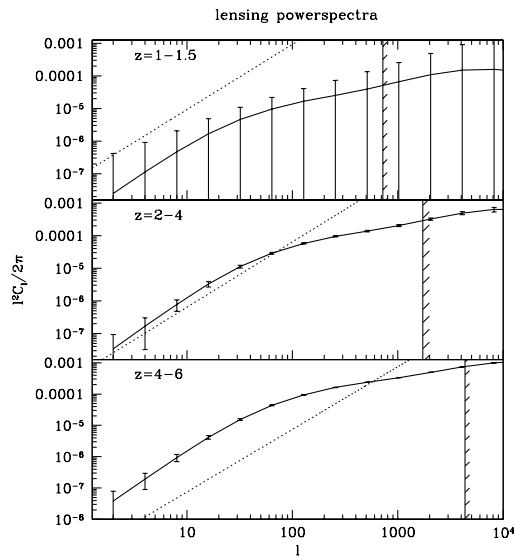


FIG. 8: The noise power spectra from the effective number densities of galaxies, compared with the lensing signals. The solid lines are the lensing power spectra. The error bars are the contribution from both the lensing reconstruction noises and the cosmic variance. The noise dominates over the signal for sources at  $z \sim 1-1.5$ , becomes comparable to but less than signal in  $z \sim 2-4$ , and further decreases at  $z \sim 4-6$ . This corresponds to a sensitivity to lens structures around  $z = 0.5, 1.0$  and  $1.5$  respectively. Note that the noise we display here is only valid for  $\ell < \ell_a$ , since we calculate  $n_g$  in the regime where the noise has similar behavior to zero mode.  $\ell_a$  are plotted as vertical lines here and in Fig. 9.

where  $\ell_s = k_s \chi(z)$  is the saturation scale that increases with redshift.  $n_g$  at different redshifts are shown in table II. Because  $n_g$  itself depends on the box-size of the simulated source and the variance of the intrinsic ellipticities  $\sigma_e^2$ , we compute  $dn_g/dz/\sigma_e^2$  instead. From the table, we see that the effective number density of galaxies increases rapidly with redshift. We also plot  $dn_g/dz/\sigma_e^2$  versus  $z$  in Fig. 7, where one can see that  $dn_g/dz/\sigma_e^2$  increases quickly with redshift. We also show the number density for a toy model where  $\Delta_{lin}^2(k_s) = 0.2$  for all redshifts.

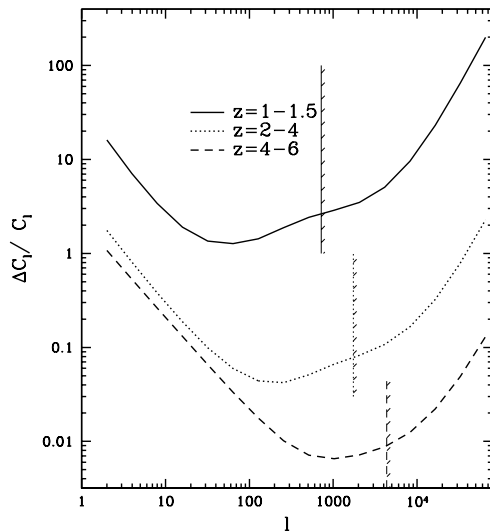


FIG. 9: The ratio of the error bars and lensing signals. The vertical lines are  $\ell_a$ , and the noise model is valid for  $\ell < \ell_a$ . For  $\ell \gg \ell_a$ , a scaling factor  $b(\ell)$  need to be applied. The calculation for  $b(\ell)$  is done in LP08, and we found it decreased from 1 gradually. Therefore the noises at these small scales will be higher than what are shown in this plot. However, these scales are not of interest to us in this paper. The error bars for 2-4 bin are at a few percents level for  $\ell \sim 20-500$ .

In Fig. 8, we compare the shot noises  $\ell^2 C_\ell^N / 2\pi$  from the effective number densities with the lensing signals. The error bars of the lensing power spectra are also plotted, which are estimated by

$$\Delta C_\ell = \sqrt{\frac{2}{(2\ell+1)\Delta\ell f_{sky}}} (C_\ell^\kappa + C_\ell^N), \quad (34)$$

where  $\Delta\ell \approx \ell/2$  because we used  $\ell = 2^n$  ( $n = 1, 2, \dots$ ) bins, and consider a half sky survey [5] with the fraction of the sky  $f_{sky} = 1/2$ . Here we assume the noise of  $\kappa$  is Gaussian, i.e., the eight-point function of temperature is Gaussian though the temperature distribution itself is

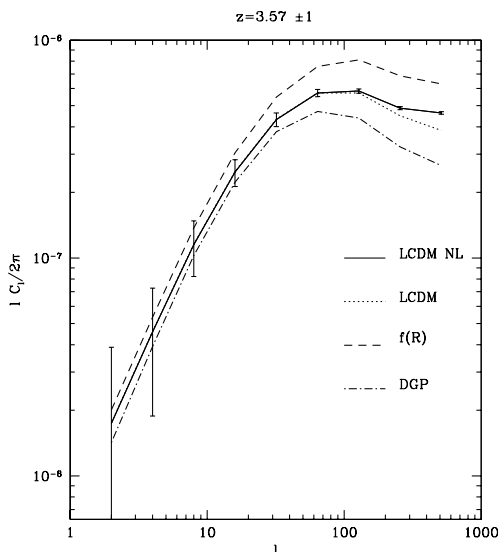


FIG. 10: The lensing power spectra from different models of dark energy (private communication with Fabian Schmidt). The average redshift is 3.57, where the effective number density of sources is calculated by interpolation with the values from Fig. 7. The error bars are calculated in the same way as Fig. 8.

non-Gaussian. Although not obvious, this point is supported by numerical tests. We also neglect the non-Gaussianity of the lensing observables themselves, which is not dominant at  $\ell < 500$  but could become an issue at higher  $\ell$  [22]. It can be seen that the noise dominates in  $z \sim 1 - 1.5$ , becomes comparable to signal in  $z \sim 2 - 4$ , and further decreases at  $z \sim 4 - 6$ . For redshift bin  $z \sim 4 - 6$ , we assume that  $dn_g/dz$  varies slowly, and use  $n_g = dn_g/dz|_{z=5}\Delta z$  with  $\Delta z = 2$ , which should provide the correct order of magnitude. Ideally, simulated sources should be generated at all redshifts between  $z = 4$  and  $z = 6$ , and the total number density is then the integral of  $dn_g/dz$  over all  $z$ . The noise is calculated similarly for  $1 - 1.25$  and  $2 - 4$  source redshift bins.

The noise is only valid for  $\ell < \ell_a \sim \ell_s$ , because we calculate  $n_g$  in the regime where the noise has a similar behavior to the zero mode. We plot  $\ell_a$  as vertical lines in Fig. 9. The full noise calculation can be done similarly to LP08, however the zero-mode  $\kappa$  calculation works well enough because we are only interested in large scales (small  $\ell$ 's). The noise at small scales will be due to the increased non-Gaussianity at lower redshifts. For  $\ell > \ell_a$ ,  $b(\ell)$  is smaller than 1, and the noise will be higher.

The relative error bars are shown in Fig. 9. The error bars for  $z \sim 2 - 4$  bin are at a few percents level for  $\ell \sim 20 - 500$ . Schmidt [23] pointed out that linear scales detection of lensing for source galaxies at  $z \sim 1 - 3$  could be a good way to distinguish three modified gravity models from a smooth dark energy:  $f(R)$  gravity, the DGP model, and the TeVeS theory. We show the lens-

ing power spectrum from different models of dark energy (private communication with Fabian Schmidt) in Fig. 10. The average redshift is 3.57, where the effective number density of sources is calculated by interpolation with the values from Fig. 7. The error bars are calculated in the same way as Fig. 8. Because of the high precision of the lensing reconstruction, we can expect to see a promising use of 21-cm sources to constrain modified gravity.

Whereas we discussed here how to use 21-cm lensing to constrain dark energy from measuring the lensing power spectrum. One can also investigate a parametrized dark energy model by constraining  $w_0, w_a$  using lensing tomography [22]. Another test of gravity and probe of dark-energy comes through the Integrated Sachs-Wolfe (ISW) effect [24]. In Fig. 11 we illustrate the potential for cross-correlating the ISW signal using the lensing of sources with  $2.5 < z < 3$ . As an illustration, we also plot the CMB lensing kernel. If the  $C_\ell$  of any of this signal is written as  $C_\ell = \int da W_\ell(a)$ , we here plot  $W_\ell(a)$  as a function of  $a$  to illustrate the sensitivity of our various probes. Whereas we see that the CMB lensing kernel overlaps widely with the ISW signal, the 21-cm lensing signal is a very good match to the ISW kernel. To quantify this, if we define as the cross-correlation coefficient between two fields X and Y as

$$r_\ell^{XY} = \sum_\ell^{\ell_{max}} C_\ell^{XY} / \sqrt{C_\ell^{XX} C_\ell^{YY}}, \quad (35)$$

we find that the cross-correlation coefficient at  $\ell = 20$  (40) for the CMB Lensing - ISW and 21-cm lensing - ISW are respectively 0.98 (0.99) and 0.95 (0.96). As such, whereas neither are perfect, the 21-cm - ISW signal is almost as good as the CMB - lensing. Using various redshift bins would help us increasing this signal [25]. By combining the different lensing sources planes, one can construct an optimal ISW estimator. This is the subject of a paper in progress.

## VI. CONCLUSION

In this paper, we discussed the possibility to constrain dark energy models with the lensing from 21-cm intensity emission at redshifts  $z \sim 1 - 6$ . First we derived the optimal quadratic estimator for non-Gaussian sources, which can be constructed numerically from simulations. Then we investigated the reconstruction noise with a large number of simulations, and revealed that there is a saturation scale for the reconstruction noise at all redshifts. We calculated the effective number densities of 21-cm sources and compared the corresponding shot noises to the lensing signals. We conclude that 21-cm sources are promising lensing sources, because they can be observed at high redshift, and may soon be mapped over half the sky [5]. The lensing reconstructed from 21-cm sources at  $z \sim 3$ , has a few percent error bars on linear scales at  $z \sim 1$ . These wide area dark matter maps are

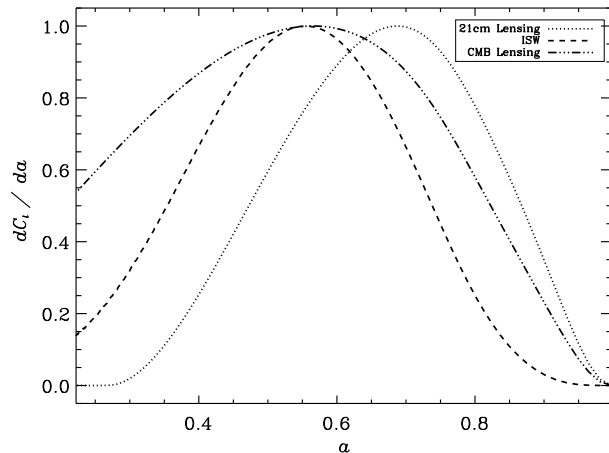


FIG. 11: We plot the kernel for  $\ell = 20$  as defined in the text for the ISW, 21-cm lensing ( $2.5 < z < 3$ ) and the CMB lensing signals as a function of the scale factor. Whereas the CMB lensing overlaps with most of the ISW signal due to its width, we also see that the 21-cm lensing at high  $z$  has a very good overlapping with the ISW kernel which suggests that the 21-cm lensing from high  $z$  constitutes a good probe of the ISW effect.

well suited to test dark energy dynamics through cross correlation with the ISW effect, and can be used to constrain modified gravity models.

*Acknowledgments* All computations were performed on the Canada Foundation for Innovation funded CITA Sunnysvale cluster. We thank Fabian Schmidt to provide the lensing power spectrum from modified gravity models in Fig. 10, and Mark Neyrinck, Tzu-Ching Chang, Joachim Harnois-Deraps for helpful discussions.

- 
- [1] R. Bean and O. Doré, Phys. Rev. D **69**, 083503 (2004), arXiv:astro-ph/0307100.
  - [2] K. M. Smith, O. Zahn, and O. Doré, Phys. Rev. D **76**, 043510 (2007), 0705.3980.
  - [3] U. Pen, New Astronomy **9**, 417 (2004).
  - [4] L. Hui, E. Gaztañaga, and M. Loverde, Phys. Rev. D **76**, 103502 (2007), 0706.1071.
  - [5] T.-C. Chang, U.-L. Pen, J. B. Peterson, and P. McDonald, Physical Review Letters **100**, 091303 (2008), arXiv:0709.3672.
  - [6] J. S. B. Wyithe, A. Loeb, and P. M. Geil, MNRAS **383**, 1195 (2008).
  - [7] M. Tegmark and M. Zaldarriaga, ArXiv e-prints (2008), 0805.4414.
  - [8] P. Zhang and U.-L. Pen, Physical Review Letters **95**, 241302 (2005), arXiv:astro-ph/0506740.
  - [9] A. Cooray, New Astronomy **9**, 173 (2004), astro-ph/0309301.
  - [10] O. Zahn and M. Zaldarriaga, Astrophys. J. **653**, 922 (2006), arXiv:astro-ph/0511547.
  - [11] R. B. Metcalf and S. D. M. White, MNRAS **381**, 447 (2007).
  - [12] T. Lu and U.-L. Pen, MNRAS **388**, 1819 (2008), arXiv:0710.1108.
  - [13] R. B. Metcalf and S. D. M. White, ArXiv e-prints **801** (2008), 0801.2571.
  - [14] C. D. Rimes and A. J. S. Hamilton, MNRAS **360**, L82 (2005), arXiv:astro-ph/0502081.
  - [15] L. Hui, E. Gaztañaga, and M. Loverde, Phys. Rev. D **77**, 063526 (2008), 0710.4191.
  - [16] M. Loverde, L. Hui, and E. Gaztañaga, Phys. Rev. D **77**, 023512 (2008), 0708.0031.
  - [17] W. Hu and T. Okamoto, Astrophys. J. **574**, 566 (2002).
  - [18] E. Bertschinger, in *New Insights into the Universe*, edited by V. J. Martinez, M. Portilla, and D. Saez (1992), vol. 408 of *Lecture Notes in Physics*, Berlin Springer Verlag, pp. 65–+.
  - [19] J. Dunkley, E. Komatsu, M. R. Nolta, D. N. Spergel, D. Larson, G. Hinshaw, L. Page, C. L. Bennett, B. Gold, N. Jarosik, et al., ArXiv e-prints (2008), 0803.0586.
  - [20] J. Harnois-Deraps, U.-L. Pen, and O. Dore, in preparation (2009).
  - [21] M. C. Neyrinck, I. Szapudi, and C. D. Rimes, MNRAS **370**, L66 (2006), arXiv:astro-ph/0604282.
  - [22] O. Dore, T. Lu, and U.-L. Pen, 0905.0501 (2009).
  - [23] F. Schmidt, Phys. Rev. D **78**, 043002 (2008), 0805.4812.
  - [24] R. K. Sachs and A. M. Wolfe, Astrophys. J. **147**, 73 (1967).
  - [25] U.-L. Pen, MNRAS **350**, 1445 (2004), arXiv:astro-ph/0402008.